Revista Brasileira de Cartografia
ISSN 1808-0936 | https://doi.org/10.14393/revbrascartogr
Sociedade Brasileira de Cartografia, Geodésia, Fotogrametria e Sensoriamento Remoto

# Study of Point Cloud Integration between UAV-based Dataset and Aerial LiDAR Survey

## *Estudo da Integração de Nuvens de Pontos entre Conjunto de Dados baseado em VANT e Levantamento Aéreo LiDAR*

Marlo Antonio Ribeiro Martins[1], Edson Aparecido Mitishita[2] e Nathan Damas Antonio[3]

1 Universidade Federal do Paraná, Pós-Graduação em Ciências Geodésicas, Curitiba, Paraná, Brasil. marlo.martins@ufpr.br.
ORCID: https://orcid.org/0000-0002-6474-6309
2 Universidade Federal do Paraná, Pós-Graduação em Ciências Geodésicas, Curitiba, Paraná, Brasil. mitishita@ufpr.br
ORCID: https://orcid.org/0000-0003-1717-7657
3 Universidade Federal do Paraná, Pós-Graduação em Ciências Geodésicas, Curitiba, Paraná, Brasil. nathandamas@ufpr.br
ORCID: https://orcid.org/0000-0002-1469-2867

Received: 01.2022 | Accepted: 11.2022

**Abstract:** The migration of Photogrammetry from the analog medium to the digital medium changed how photogrammetric surveys were carried out and how data are processed, allowing the automation of several steps used in the photogrammetric design workflow. There is extensive research in cartographic and geodetic sciences, involving the acquisition of data through photogrammetry, and through techniques such as Structure from Motion (SfM) and Laser Scanner survey. Such research and work involve the use of point clouds from Unmanned Aerial Vehicle (UAV) photogrammetric surveys and Terrestrial Laser Scanner (TLS) surveys, as well as the fusion of these point clouds. This work aims to study the integration of an aerial LiDAR point cloud with a Photogrammetric Point Cloud (PPC) from the UAV survey to minimize occlusion failures and building edges, densify the point cloud, and reduce spurious points. Statistical analyses were performed for the refinement, adjustment, and integration between the point clouds. The results showed that the correction map generated for integrating the clouds reached the objective proposed in this work. The integration of clouds increased from 7 pts/m² of the cloud coming from LiDAR to 140 pts/m² in the final.
**Keywords:** LiDAR Point Cloud (PCL). Photogrammetric Point Cloud (PPC). Correction Map.

**Resumo**: A migração da Fotogrametria do meio analógico para o meio digital, alterou a maneira como os levantamentos fotogramétricos são realizados, bem como, os dados eram processados, permitindo a automatização de diversas etapas empregadas no fluxo de trabalho do projeto fotogramétrico. Existe uma extensa pesquisa nas ciências cartográficas e geodésicas, envolvendo a aquisição de dados por meio da Fotogrametria, e por meio de técnicas como o *Structure from Motion* (SfM) e o levantamento Laser Scanner. Tais pesquisas e trabalhos envolvem a utilização de nuvens de pontos oriundas do levantamento fotogramétrico de Veículo Aéreo Não Tripulado (VANT) e do Laser Scanner Terrestre (LST), bem como, a fusão dessas nuvens de pontos. O objetivo deste trabalho é integração de uma nuvem de pontos LiDAR aéreo com uma nuvem de pontos provinda do levantamento fotogramétrico VANT, visando minimizar as falhas de oclusão e bordas das edificações, densificar a nuvem de pontos e reduzir os pontos espúrios. Foram realizadas análises estatísticas para o refinamento, ajustamento e integração entre as nuvens de pontos. Os resultados mostraram que o mapa de correção gerado para a integração entre as nuvens atingiu o objetivo proposto nesse trabalho. A integração das nuvens de pontos resultou em um aumento de 7 pts/m² da nuvem provinda do LiDAR para 140 pts/m² na nuvem resultante final.
**Palavras-chave:** Nuvem de Pontos LiDAR (PCL). Nuvem de Pontos fotogramétrica (PPC). Mapa de Correção.

## 1 INTRODUCTION

The migration of Photogrammetry, from analog to digital, changed how photogrammetric surveys were carried out and the data processed, allowing the automation of several steps used in the photogrammetric design workflow. As an alternative to conventional platforms for sensor boarding, numerous more affordable options were used, from kites to the latest Unmanned Aerial Vehicles (UAV). However, initially, due to the limitations of these platforms, it was not possible to obtain results that exceeded centimeter accuracy, thus

limiting the application of these low-cost surveys (SMITH et al., 2009).

Other fields of science have evolved, collaborating with measurement procedures using images. In computer vision, algorithms have been developed to facilitate and optimize digital image processing. At the intersection of these two areas of knowledge (Photogrammetry and Computer Vision), Ullman (1979) created the technique called Structure from Motion (SfM). According to Westoby et al. (2012), this technique was developed to estimate the three-dimensional structure of objects from images without requiring a priori knowledge of the sensor's position or orientation when taking photographs, nor for knowledge of the three-dimensional coordinates of the points on the physical surface. In the middle of the last decade, Snavely, Seitz and Szeliski (2006, 2008) researched the use of SfM to model heritage sites around the globe, such as Mount Rushmore, the Coliseum, and the Great Wall of China.

The use of UAVs as a low-cost aerial platform, together with the SfM algorithm, for carrying out photogrammetric surveys has lately stood out both in the engineering market and academia. Additionally, LiDAR technology, has been widely used in mapping cities, integrated with digital photogrammetric images, from the beginning of the 21st century (SZABÓ et al., 2016). However, LiDAR data frequently present occlusions, shadows, and failure due to irregularity in the generated point clouds, which can be considered a deficiency in reproducing complete surface models (LESLAR, 2015). In this segment, UAV technology can be used with high performance to overcome these deficiencies, mainly because these platforms are relatively cheap and easy to operate (LESLAR, 2015). The use of remoted piloted platforms has become much more practical and commonplace with the technology revolution that has emerged in recent decades. At the end of the last century, the automatic reconstruction of three-dimensional urban settings became important for photogrammetric research (GRUEN; BALTSAVIAS; HENRICSSON, 1997; GRUEN; KUEBLER; AGOURIS, 1995).

The articles published since these beginnings were numerous, in addition to investigating various methods of reconstruction enabling a series of approaches to commercial services and software (BRENNER, 2005). Habib, Zhal and Kim (2010) presented the important statement: "the generation of digital models of complex structures remains a challenge." In the past, the difficulties and operational cost of extracting three-dimensional information from buildings using photogrammetric images were the main factors that motivated the increase in the use of 3D point clouds generated from a laser as an alternative data source.

Considering this context and the fact that few studies address the integration of point clouds from aerial platforms, like LiDAR and data from UAV, this research proposes the integration of point clouds from different sources to implement the three-dimensional reconstruction of buildings. These sources are the LiDAR and "Structure from Motion" (SfM) point clouds. This integration seeks to densify the LiDAR point cloud in areas with point failures due to occlusions and irregularity of points, mainly on the edges of buildings. The search for a methodology capable of integrating the LiDAR survey dataset with a dataset from Photogrammetry proved to be an important topic in this field of knowledge. According to Shan and Toth (2018), constant technological evolution is increasingly making it possible to collect geoinformation from multiple sensors at a more and more affordable cost.

Kwon et al. (2017) proposed a method to generate a 3D point cloud using a hybrid scanning method. The study proposed by the authors aimed to present a hybrid digitization method for 3D earthwork modeling in construction operations. The authors observed that the hybrid scanning method proposed in the study enabled them to quickly and accurately process the 3D mapping of atypical soil shapes that change continuously according to the construction situation. Moon et al. (2018) proposed a methodology for the generation and merging of hybrid point cloud data acquired by TLS and by UAV-based image processing. A comparison was also made between the data sets acquired in laser scanning and image processing, using some case studies involving the planning of heavy equipment for civil construction and earthmoving. Finally, an analytical comparison was made to verify the accuracy of UAV-based image processing technology for earthmoving projects. According to the authors, the study confirmed the usability of photogrammetric data for this work type and proposed a methodology. Šašak et al. (2019) presented a new methodological approach based on the combined use of TLS imaging and short-range photogrammetry of a UAV to generate a high-resolution point cloud and a digital elevation model of rugged terrain in the alps. This approach was demonstrated in a small study area at the top of a thawed valley in the Tatras Mountains, Slovakia. The results showed that the complementation of the point cloud generated by the TLS with the UAV point cloud supplemented the coverage made by the first technique in places with insufficient coverage and reduced the occlusions present in the 3D point cloud. The authors stated that this technique allows the 3D mapping of steep slopes and protruding ledges present in mountainous terrain.

As we can see, there is extensive research in cartographic and geodetic sciences involving the acquisition of data from reality, using Photogrammetry through techniques such as Structure from Motion (SfM) and the Laser Scanner survey. However, these researches and works involve using point clouds from

the short-range Photogrammetry survey (UAV and SfM) and the TLS, and the union and fusion of these point clouds. In this sense, there is a need for studies investigating the accuracy of the union of point clouds from Airbone Laser Scanner surveys and point clouds from SfM techniques. The first part of this research was published in Martins and Mitishita (2021), presenting a methodology to extract three-dimensional coordinates from the LIDAR point cloud. This survey was used to verify the accuracy of point entities extracted by Linear Regression and Line Intersection. Thus, this work aims to develop a theoretical study and practical procedures for realizing the union of point clouds from different origins, using specialist software.

## 2 MATERIALS AND METHODS

### 2.1 Research Area

The research area and the aerial survey is located in the urban area of Curitiba-PR, in the City Industrial district. Figure 1a shows the location map of the study area and 1b shows the study area where the UAV survey was carried out in greater detail.

Figure 1 – (a) Study Area Location – (b) UAV Study Area.

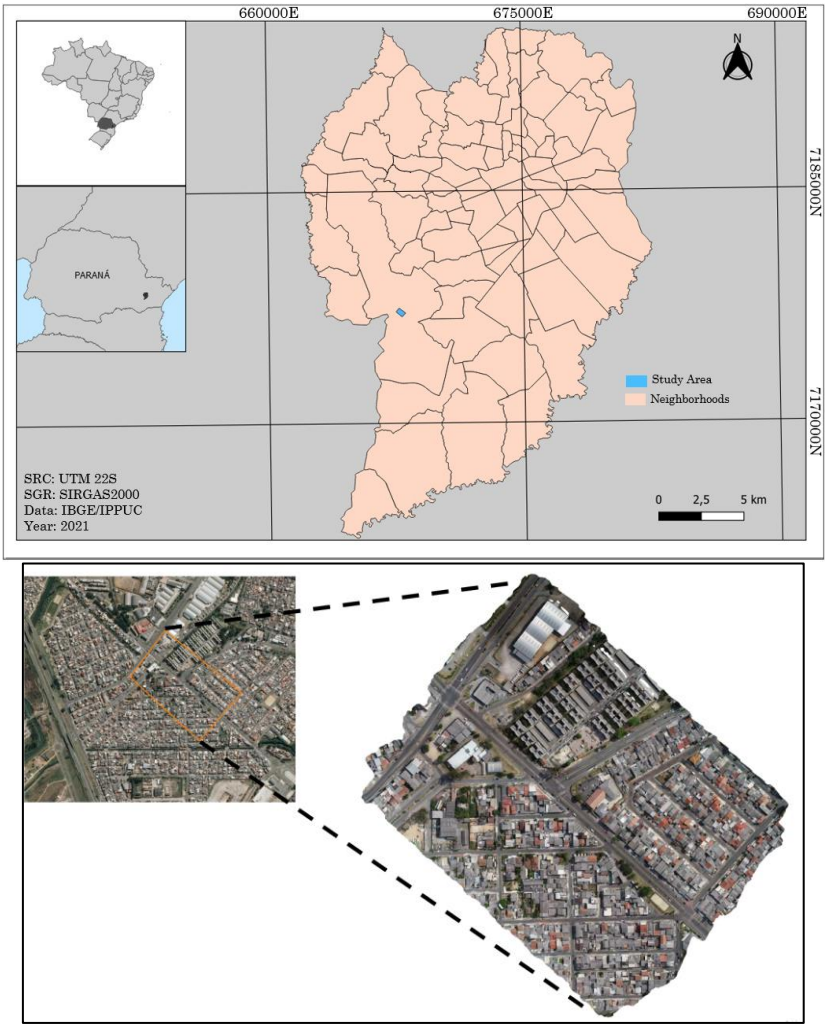


(b)

Source: Authors (2021).

### 2.2 Methods

The methods proposed for carrying out this research are represented in schematic form and summarized in the flowchart of Figure 2. The proposed methodology for this work was divided into three main parts: the first part is the acquisition of data, the second part is the data processing, and the third and last part, comprises the fusion of point clouds.

Figure 2 – Steps of Research Methodology.

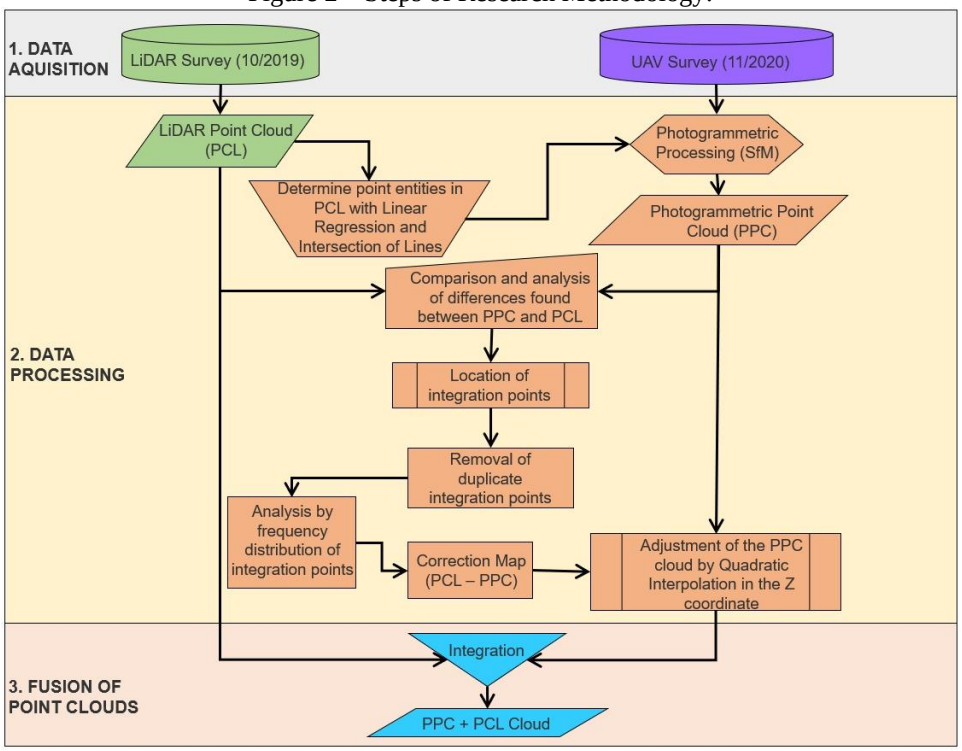


Source: Authors (2021).

### 2.2.1 LIDAR AERIAL SURVEY

The LiDAR aerial survey in the study area corresponds to the municipality of Curitiba-PR. The survey mentioned above consists of two adjacent strips in the North-South direction, carried out in October 2019 by the Institute of Research and Urban Planning of Curitiba (IPPUC). The equipment used was the Optech Pegasus HD500 Laser Scanner, has an Applanix POS AV 510 Inertial Measurement Unit with absolute positional accuracy of <0.1m, of <0.005° in Roll and Pitch and of <0.08 in Yaw. The average collection density is 6 points/m². The format for recording the data was ".LAS,". The set of points sampled over the study area for this work, i.e., the LiDAR point cloud, was here called Point Cloud LiDAR (PCL).

### 2.2.2 DETERMINATION OF PHOTOGRAMMETRIC SUPPORT POINTS

In this step, the photogrammetric support points were determined by applying the methodology of extracting three-dimensional coordinates of point entities from a LiDAR point cloud in an urban region using Linear Regression and Line Intersection (MARTINS; MITISHITA, 2020). The results obtained in the experiments carried out in this study show that the proposed Linear Regression and Line Intersection method for the extraction of point entities in a LiDAR point cloud can be recommended in critical engineering applications for use in photogrammetric mapping processes in PEC-PPC scales, Class A of 1/2.000, and below (MARTINS; MITISHITA, 2020).

### 2.2.3 UAV AERIAL SURVEY AND PHOTOGRAMMETRIC PROCESSING

The aerial survey was carried out in November 2020, using a Phantom 4 PRO, see Figure 1, as a platform for acquiring aerial images. Photos of the study area were captured with a flight height of 114 m, resulting in a 2.6 cm mean pixel size over the ground (GSD). In total, 181 images of the study area were captured, with 40% lateral and 70% frontal overlapping.

For processing photogrammetric with the SfM technique, the only parameter provided by the manufacturer is the focal length, 8.8 mm. The processing adopted the Conrady-Brown model for the interior orientation of the sensor. The photogrammetric observations of the connection points, i.e., tie points, are made by the scale-invariant feature transformation algorithm, better known as SIFT. The 12 control points were

included aiming at the integration of the LiDAR and UAV point clouds, mainly in the planimetric part, i.e., 12 point entities extracted from the LiDAR cloud, according to the methodology presented in Martins and Mitishita (2021), and types illustrated in Figure 3a. Figure 3b illustrates the types of point entities employed as support points for SfM photogrammetric processing.

Figure 3 – (a) Obtaining the Point Entities; (b) Control Points.

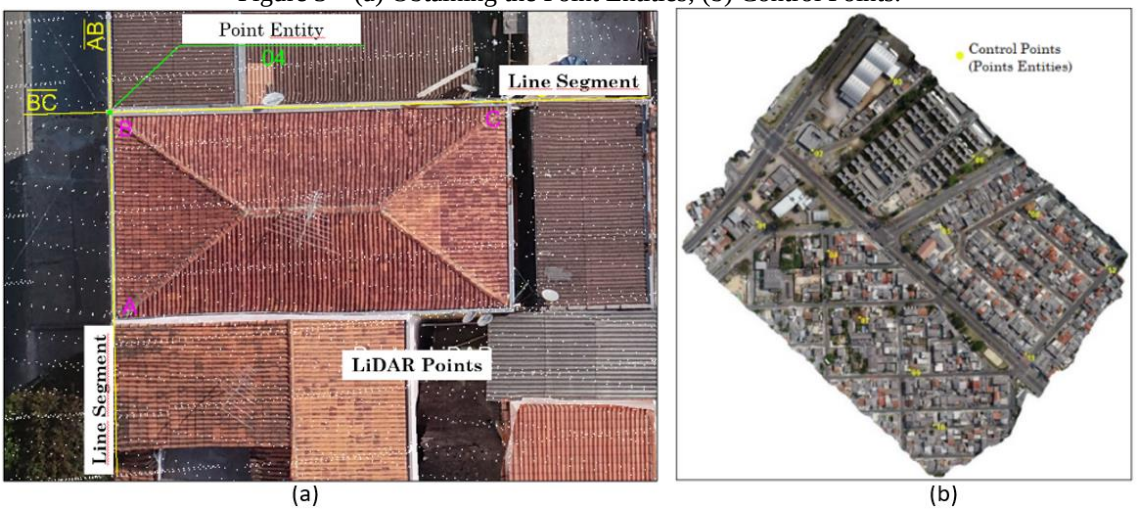


Source: Authors (2021).

The point cloud densification is done using Multi-View Stereo (MVS) algorithms. MVS is a term given to a group of techniques that use more than two images and stereo correspondence as their main cue (FURUKAWA; HERNÁNDEZ, 2015). The MVS algorithm makes it possible to increase the number of points of the sparse cloud, enabling a three-dimensional reconstruction of the surface with greater quality and less noise. With the sparse cloud densification, the UAV points cloud is generated that will be used from that point in the research as Photogrammetric Point Cloud (PPC) in the ".LAS" format.

### 2.2.4 COMPARISON OF DIFFERENCES FOUND BETWEEN PPC AND PCL

With the two-point clouds, PCL and PPC, processed, the next step consisted of analyzing their differences. Since the point cloud originating from LiDAR is considered the field truth, i.e., it will be taken as a reference, the operations to be carried out will be performed on the point cloud originating from the UAV, the PPC. The differences between the two-point clouds were analyzed semi-automatically by checking the differences presented along the PPC and PCL. As shown in Figure 4, the discrepancies between the two clouds were more evident in the altimetric axis (Z coordinate). The detection of planimetric alignment was performed manually, observing the representation of the features of roofs and their corners in the point clouds and their alignment relative to each other.

Figure 4 - Discrepancies found between the two Point Clouds.

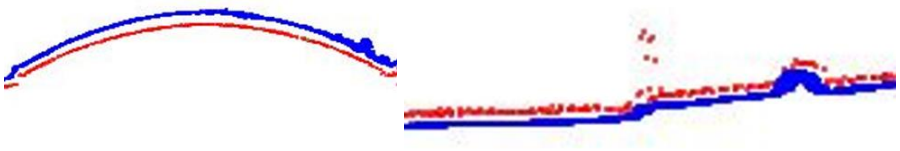

Source: Authors (2021).

### 2.2.5 SEARCH FOR INTEGRATION POINTS

The points on the PPC planimetrically close to the points on the PCL were automatically identified. The criterion used to define the proximity is the point on the PPC, and the point on the PCL be apart at most 1 cm (Figure 5a) since the accuracy of the surveys is in the order of centimeters. Thus, the step consisted of identifying points on the PPC that had the same planimetric coordinates on the PCL, that is, planimetrically

coincident points, henceforth called integration. The integration points in PPC and PCL were filtered automatically in the TerraScan software, returning the values of the planimetric coordinates of the integration points, which were exported to a new cloud of integration points PCL+PDC (Figure 5b).

Figure 5 – (a) Identification of Integration Points; (b) Integration Points Cloud PCL + PPC.

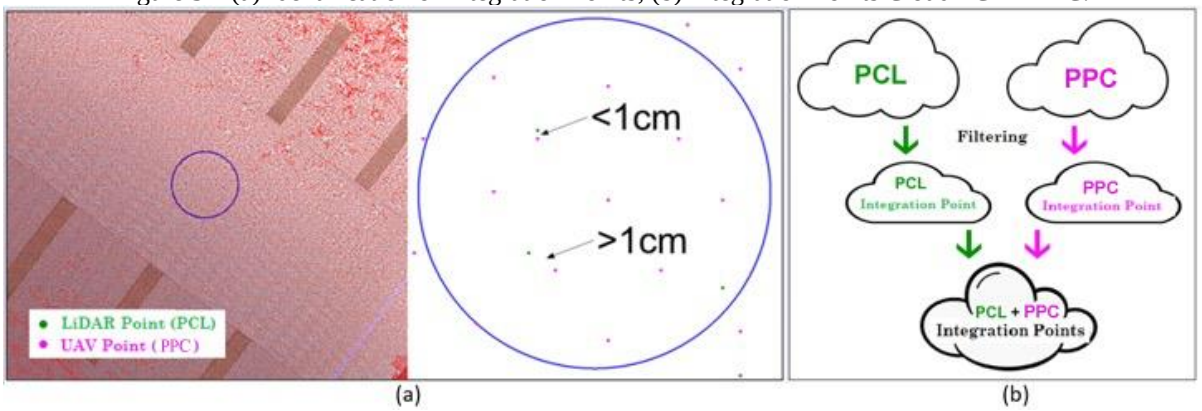


Source: Authors (2021).

### 2.2.6 REMOVAL OF DUPLICATE INTEGRATION POINTS

The duplication of integration points resulting from the PPC and PCL clouds was removed at this methodology step. This operation allowed us to observe that the result of the points coming from the UAV presented more than one point with equal coordinates in the planimetry. After performing the search in the PPC, the same point was returned more than once to the PCL. Solving this issue required cleaning these data, thus eliminating the points that appeared more than once in the PPC results.

PPC points were classified based on the calculation of the two-dimensional Euclidean distance of the plane coordinates of its points, resulting from the search for homologous points from the previous step. The criterion applied to classify the points was as follows: if d=0, i.e., if the coordinates of a point p on line i were equal to a point q on line j, this point would be classified with the value “REPEATED.” If not, if d≠0, the value assigned for the classification would be “CORRECT.”

### 2.2.7 ASSESSMENT BY THE FREQUENCY DISTRIBUTION OF INTEGRATION POINTS

The first step to carry out the statistical evaluation by frequency distribution is removing planimetrically coincident points, but altimetrically have a distance greater than three standard deviations (see Figure 6).

Figure 6 – Removed Integration Points in PPC Integration points with the same planimetric position.

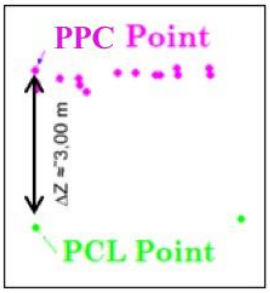


Source: Authors (2021).

Such points are statistically considered gross errors. These points will be removed from the integration points not to alter the statistical analysis, as they do not represent the integration of clouds. The objective of this step was to improve the results so that a correction map between the PCL and PPC clouds could be generated later. With the integration points organized in a table, the frequency distribution (absolute and relative) of the discrepancies resulting from the previous step was analyzed. Data classification used classes of values to obtain the frequency table. The criterion to define the classes was the Sturges Rule (Log Rule) for

determining the number of classes and the interval between these classes. Position and Dispersion measures (e.g. Median, Mean, Std. Dev., Variance) were calculated to find values that summarize data variability.

### 2.2.8 GENERATION OF THE CORRECTION MAP BETWEEN PPC AND PCL

The previous step allowed the integration point cloud to be appropriately filtered and cleaned. The analyses enabled removing repeated points when filtering the integration points between PPC and PCL clouds. Applying these methods to the integration cloud generated two tables: the first (Table 1) with coordinates (E, N, H) of the PCL and PPC clouds and the second (Table 2) with only the coordinates (E, N, ΔH) for the generation of the correction map between PPC and PCL (Figure 7).

Figure 7 – Altimetric Difference of Correction Map Points.

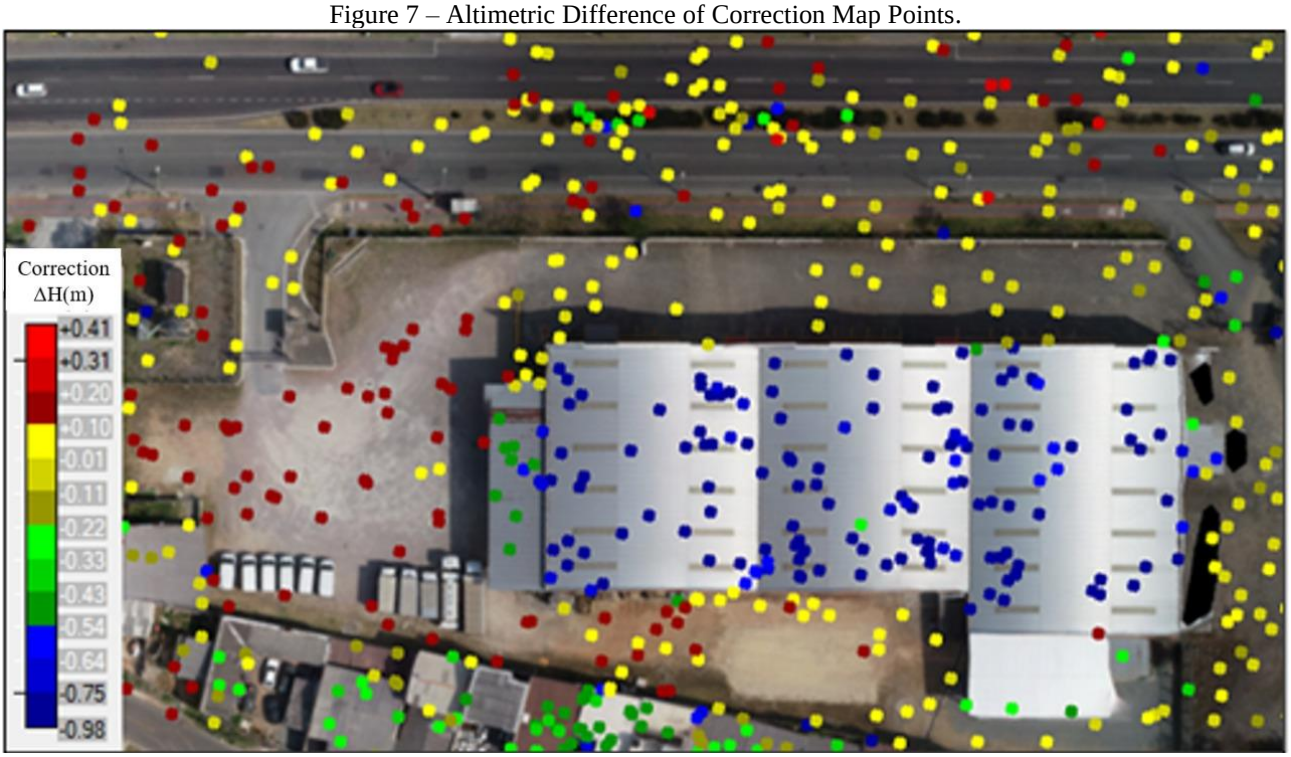


Source: Authors (2021).

Table 1 – Integration Cloud Example.

| Position | PCL (LiDAR Cloud) | | | PPC (UAV Cloud) | | | Correction ΔH (m) |
|---|---|---|---|---|---|---|---|
| | E (m) | N (m) | H (m) | E (m) | N (m) | H (m) | |
| Ground | 667,432.06 | 7,177,176.20 | 887.72 | 667,432.06 | 7,177,176.20 | 887.50 | 0.22 |
| Roof | 667,432.73 | 7,177,179.25 | 887.46 | 667,432.73 | 7,177,179.25 | 888.41 | -0.95 |

Source: Authors (2021).

Table 2 – Example of Points Used for the Correction Map

| Position | Correction | | |
|---|---|---|---|
| | E (m) | N (m) | ΔH (m) |
| Ground | 667,432.06 | 7,177,176.20 | 0.22 |
| Roof | 667,432.73 | 7,177,179.25 | -0.95 |

Source: Authors (2021).

### 2.2.9 APPLICATION OF THE CORRECTION MAP TO THE PPC CLOUD

After applying the statistical analysis by frequency distribution and generating the correction map. From this map a quadratic interpolation in the altimetric coordinates was applied to adjust the PPC cloud. In order to use this correction map, a program was developed to enter the PPC cloud and the correction map file, having as final file the PPC cloud adjusted in relation to the PCL cloud (Figure 8). The quadratic interpolation method used in this research was polynomials.

Figure 8 - Quadratic Interpolation Software.

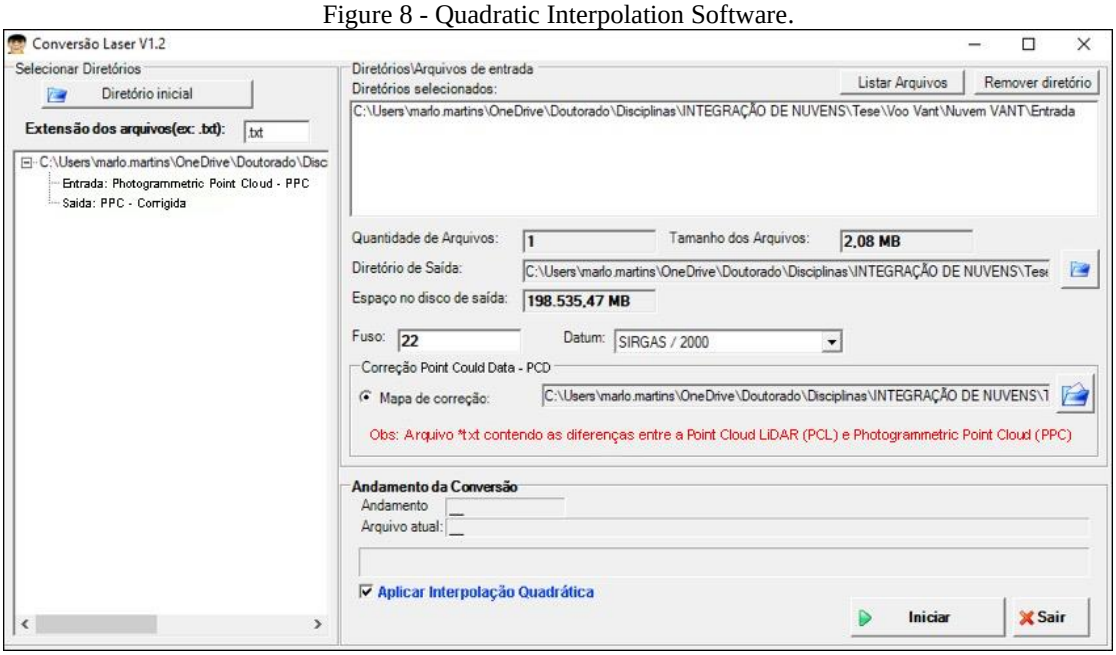


Source: Authors (2021).

### 2.2.10 INTEGRATION OF POINT CLOUDS

The third and last part of the proposed methodology refers to the fusion of point clouds. This step applies the correction map generated previously in the point cloud originating from the UAV to adjust it in the LiDAR point cloud. The altimetric coordinates of adjustment of the homologous points were calculated by quadratic interpolation. These corrections were applied in the PPC cloud to fit them with the PCL, as shown in the Results and Discussions chapter.

## 3 RESULTS AND DISCUSSIONS

This study will present the results that discuss the fusion of PPC and PCL point clouds in detail. The results obtained in determining photogrammetric support points were presented and discussed in Martins and Mitishita (2021).

## 3.1 Results for Integration of LiDAR and UAV Clouds

### 3.1.1 PHOTOGRAMMETRIC PROCESSING RESULTS

Using the methodology and results presented in Martins and Mitishita (2021), point entities were obtained in the PCL cloud (Table 3) to be employed as control points in the photogrammetric processing. This procedure eliminates the need to survey topographic points by GNSS.

Table 3 – Point Entities obtained from the PCL.

| **Control Points** (Point Entities) | **E (m)** | **N (m)** | **H (m)** |
|---|---|---|---|
| 01 | 667,541.66 | 7,177,212.74 | 891.83 |
| 02 | 667,623.63 | 7,177,318.44 | 892.80 |
| 03 | 667,742.87 | 7,177,426.23 | 892.06 |
| 04 | 667,647.88 | 7,177,169.01 | 891.69 |
| 05 | 667,816.22 | 7,177,204.87 | 897.35 |
| 06 | 667,864.90 | 7,177,311.48 | 898.32 |
| 07 | 667,694.01 | 7,177,069.10 | 889.27 |
| 08 | 667,948.77 | 7,177,226.12 | 901.05 |
| 09 | 667,769.40 | 7,176,990.97 | 892.08 |
| 10 | 667,805.45 | 7,176,907.52 | 891.44 |
| 11 | 667,943.17 | 7,177,015.72 | 894.59 |
| 12 | 668,063.40 | 7,177,147.48 | 901.32 |

Source: Authors (2021).

The distribution of these points will show after. These specific entities also ensure that the PCL and PPC cloud are planimetrically compatible, thus completing the first integration step. The values of the interior orientation of the sensor, considering the Interior Orientation Parameters (IOP) and their respective standard deviations, estimated in the self-calibration processes are presented in the table below (Table 4).

Table 4 – Estimated IOP in autocalibration.

| IOP | Value (pixel) | Std. Dev. (pixel) |
|---|---|---|
| F | 4031.15 | 2.10 |
| Cx | -1.55 | 0.04 |
| Cy | 21.16 | 0.05 |
| K1 | $2.33x10^{-3}$ | $3.4x10^{-5}$ |
| K2 | $-9.83x10^{-3}$ | $1.20x10^{-4}$ |
| K3 | $01.36x10^{-2}$ | $1.30x10^{-4}$ |
| P1 | $6.79x10^{-4}$ | $2.10x10^{-6}$ |
| P2 | $-2.89x10^{-4}$ | $1.50x10^{-6}$ |

Source: Authors (2021).

The high correlation of the IOPs can explain the significantly high value for the focal length with the CP coordinates, especially the focal length with the Z0 coordinate. Subsequently, the spatial distribution of the control points and general accuracy of the processing can be seen in Table 5 and Figure 9. Table 6 presents the discrepancies of the 12 individualized control points. The results show the central values related to this discrepancy, such as the mean quadratic error (RMSE) for the X, Y, and X, Y, and Z coordinates.

Table 5 – General RMSE of control points

| RMSE (m) | | | |
|---|---|---|---|
| **X** | **Y** | **XY** | **Z** |
| 0.029 | 0.016 | 0.034 | 0.042 |

Source: Authors (2021).

Figure 9 – Distribution of Control Points with Residuals.

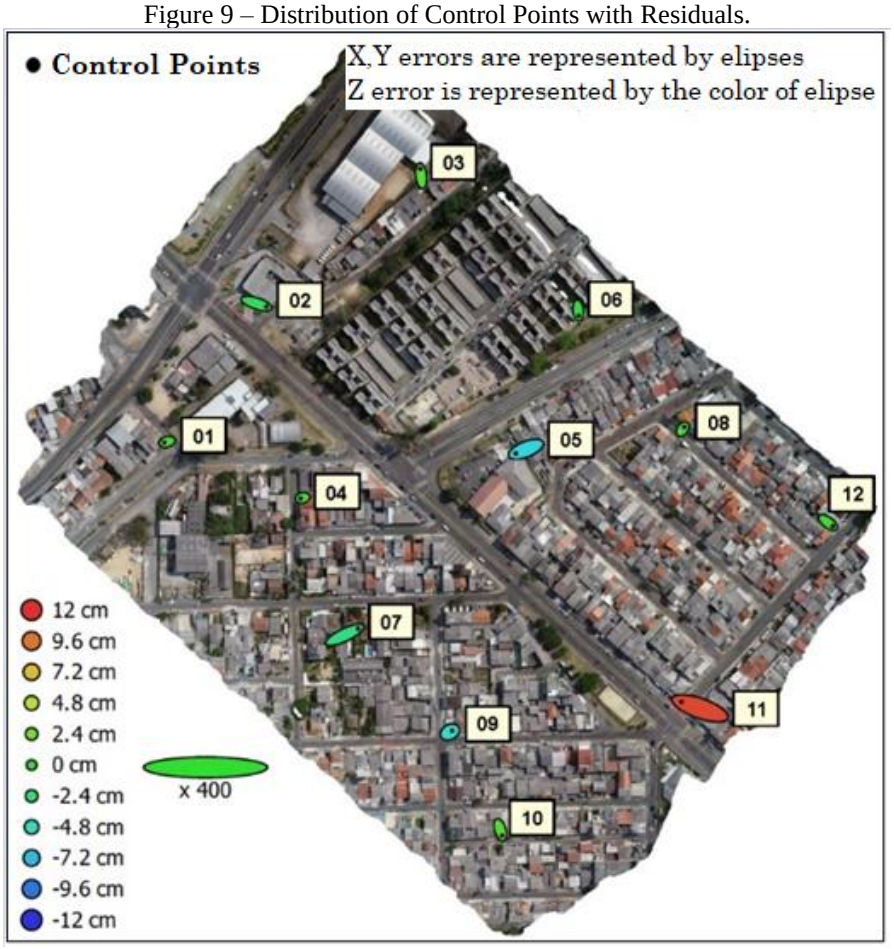


Source: Authors (2021).

Table 6 – RMSE of Control Points.

| RMSE (m) | | | | |
|---|---|---|---|---|
| **Point** | **E** | **N** | **H** | **Total** |
| 01 | -0.0101 | -0.0029 | 0.0057 | 0.0119 |
| 02 | 0.0364 | -0.0117 | -0.0134 | 0.0405 |
| 03 | -0.0031 | 0.0261 | 0.0123 | 0.029 |
| 04 | -0.0073 | -0.0019 | 0.0081 | 0.011 |
| 05 | -0.037 | -0.0151 | -0.0625 | 0.0742 |
| 06 | 0.0018 | -0.0193 | -0.0052 | 0.0201 |
| 07 | 0.0489 | 0.0229 | -0.0284 | 0.061 |
| 08 | 0.0057 | 0.0077 | 0.0087 | 0.013 |
| 09 | 0.0081 | 0.0049 | -0.0546 | 0.0554 |
| 10 | 0.0065 | -0.0207 | 0.0128 | 0.0252 |
| 11 | -0.068 | 0.0237 | 0.1121 | 0.1332 |
| 12 | 0.018 | -0.0136 | 0.0043 | 0.023 |

Source: Authors (2021).

### 3.1.2 ANALYSIS AND COMPARISON OF DIFFERENCES FOUND BETWEEN PPC AND PCL

The differences between the two-point clouds were analyzed through the visual verification presented along the PPC and PCL. Figure 10 shows that the differences found during the analysis of the point clouds remained approximately within a constant threshold. The PPC cloud (in blue), when compared with the PCL (in red) in the soil region, showed a negative discrepancy of approximately twenty centimeters. As for the roof region, the points on the PPC presented a positive discrepancy of approximately one meter.

Figure 10 – Mean differences found throughout PPC compared to PCL.

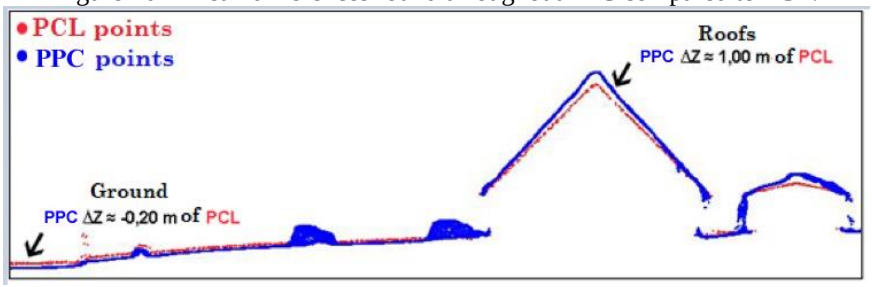


Source: Authors (2021).

The comparison between PCL and PPC clouds using point entities extracted from the LiDAR cloud (PCL) as a control point indicated they present altimetric differences. The entities managed to solve only the UAV cloud planimetry (PPC), as shown in Figure 9. Thus, one of the possible causes of this problem is performing aerial surveys by UAV, as the cameras used in this equipment have very small focal lengths, which can cause this scale effect in the altimetry of UAV clouds.

### 3.1.3 RESULTS OF THE LOCATION OF HOMOLOGOUS POINTS IN PLANIMETRY

The location of the homologous points in the PPC point cloud was performed semi-automatically and returned the values of the planimetric coordinates of the points identified as homologous, which were exported to a text file. Table 7 shows an example of the search carried out by homologous points for the location of the selected study area. The UAV cloud had a total of 15,535 points, and the LiDAR cloud had a total of 14,125 points. Since the PCL points are considered field truth, they were used as a reference to search. In Table 7, the numbers highlighted show the homologous points in the PPC cloud that were filtered.

Table 7 - Sample of Planimetrically Homologous Points located in both clouds.

| **PCL (LiDAR Cloud) – 14,215 Pts** | | | **PPC (UAV Cloud) – 15,535 Pts** | | |
|---|---|---|---|---|---|
| **E (m)** | **N (m)** | **H (m)** | **E (m)** | **N (m)** | **H (m)** |
| 667,441.68 | 7,177,225.61 | 887.39 | 667,441.68 | 7,177,225.61 | 887.63 |
| | | | **667,441.68** | **7,177,225.61** | **887.63** |
| | | | **667,441.68** | **7,177,225.61** | **887.63** |
| | | | **667,441.68** | **7,177,225.61** | **887.63** |
| 667,442.25 | 7,177,226.76 | 887.40 | 667,442.25 | 7,177,226.76 | 887.55 |

Source: Authors (2021).

### 3.1.4 RESULTS OF REMOVAL OF DUPLICATE INTEGRATION POINTS

This step removed the points that present duplication in the PPC cloud, according to topic 2.2.6. Table 8 shows an example of this duplication of points. The points with the same planimetric coordinates were classified as "REPEATED," and the points in the PPC with different coordinates were classified as "CORRECT." The class "REPEATED" points were eliminated, leaving only the class "CORRECT." It is worth mentioning that after this removal of the repeated points, there was a reduction of approximately 8.5% of the integration points in the PPC cloud.

Table 8 - Example of the classification used in the filtered points of the PPC.

| **LiDAR (PCL)** | | **UAV (PPC)** | | Class |
|---|---|---|---|---|
| **E (m)** | **N (m)** | **E (m)** | **N (m)** | |
| 667,441.68 | 7,177,225.61 | 667,441.68 | 7,177,225.61 | CORRECT |
| | | **667,441.68** | **7,177,225.61** | **REPEATED** |
| 667,442.25 | 7,177,226.76 | 667,442.25 | 7,177,226.76 | CORRECT |

Source: Authors (2021).

### 3.1.5 STATISTICAL ANALYSIS OF INTEGRATION POINTS

After this reduction of duplicate points, a new removal of points was carried out according to topic 2.2.7. Thus, the values eliminated in this step presented a discrepancy greater than +/-1.38 m since the standard deviation of all altimetric discrepancies was +/- 0.46 cm. With this removal of points, the PCL and PPC clouds had 11,420 points each, i.e., a reduction of 24.5%. After this statistical removal, the frequency distribution was performed for the integration points and organized in Table 9.

Table 9 – Frequency Distribution of Discrepancies.

| **Classes (m)** | | | | **Mean Point (m)** | **Absolut** | **Relative (%)** | **Abs. Accum.** | **Rel. Accum. (%)** |
|---|---|---|---|---|---|---|---|---|
| 1ª | -1.38 | \|----- | -1.18 | -1.28 | 171 | 1.49% | 171 | 1.49% |
| 2ª | -1.18 | \|----- | -0.98 | -1.08 | 388 | 3.44% | 388 | 3.44% |
| 3ª | -0.98 | \|----- | -0.78 | -0.88 | 754 | 6.68% | 1142 | 10.12% |
| 4ª | -0.78 | \|----- | -0.58 | -0.68 | 767 | 6.79% | 1909 | 16.91% |
| 5ª | -0.58 | \|----- | -0.38 | -0.48 | 1226 | 10.86% | 3135 | 27.77% |
| 6ª | -0.38 | \|----- | -0.18 | -0.28 | 1879 | 16.64% | 5014 | 44.41% |
| 7ª | -0.18 | \|----- | 0.02 | -0.08 | 2104 | 18.63% | 7118 | 63.04% |
| 8ª | 0.02 | \|----- | 0.22 | 0.12 | 2293 | 20.31% | 9411 | 83.35% |
| 9ª | 0.22 | \|----- | 0.42 | 0.32 | 1097 | 9.72% | 10508 | 93.07% |
| 10ª | 0.42 | \|----- | 0.62 | 0.52 | 408 | 3.61% | 10916 | 96.68% |
| 11ª | 0.62 | \|----- | 0.82 | 0.72 | 138 | 1.22% | 11054 | 97.90% |
| 12ª | 0.82 | \|----- | 1.02 | 0.92 | 83 | 0.74% | 11137 | 98.64% |
| 13ª | 1.02 | \|----- | 1.22 | 1.12 | 86 | 0.76% | 11223 | 99.40% |
| 14ª | 1.22 | \|----- | 1.42 | 1.32 | 68 | 0.60% | 11291 | 100.00% |

Source: Authors (2021).

Table 9 shows that a total of 14 classes were calculated by the Sturges rule, starting at -1.38 and going to 1.41 meters, with an interval between classes of 0.20 m. The highest absolute frequency values can be observed between the third and tenth classes. These values represent a total of 88.3% of the data, i.e., considering the values that are not between the third and tenth class, we have a frequency absolute of 11,7%. Figure 11 illustrates the chart of the frequency distribution of discrepancies.

Figure 11 – Frequency Distribution Chart of Discrepancies.

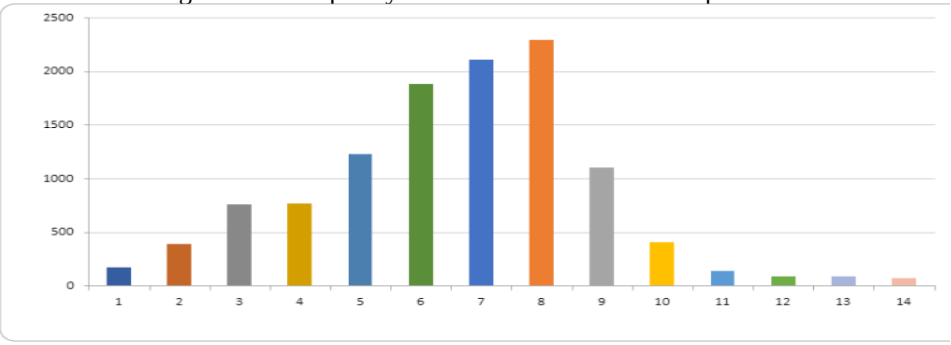


Source: Authors (2021).

We can observe that the highest frequency of discrepancies values is found in classes 6, 7, and 8, which range from -0.38 to 0.22 m. For the position measures, arithmetic mean, median, and mode are -0.17 m, -0.13 m, and 0.12 m, respectively, distributed among these three classes mentioned above. As for the dispersion measures, the mean deviation, standard deviation, maximum error, and variance values are, respectively, 0.36 m, 0.46 m, and 1.38 m.

Since only a small percentage of discrepancies were concentrated at the edges of the distribution (11.7%), one more data filtering was performed to refine the results. The data from the edges were deleted, and a new frequency distribution table was generated (Table 10).

Table 10 – Refined Discrepancies Frequency Distribution.

| Classes (m) | | | | Mean Point (m) | Absolut | Relative (%) | Abs. Accum. | Rel. Accum. (%) |
|---|---|---|---|---|---|---|---|---|
| 1ª | -0.98 | \|----- | -0.78 | -0.88 | 754 | 7.45% | 754 | 7.45% |
| 2ª | -0.78 | \|----- | -0.58 | -0.68 | 767 | 7.58% | 1521 | 15.03% |
| 3ª | -0.58 | \|----- | -0.38 | -0.48 | 1226 | 12.11% | 2747 | 27.14% |
| 4ª | -0.38 | \|----- | -0.18 | -0.28 | 1879 | 18.57% | 4626 | 45.71% |
| 5ª | -0.18 | \|----- | 0.02 | -0.08 | 2104 | 20.79% | 6730 | 66.50% |
| 6ª | 0.02 | \|----- | 0.22 | 0.12 | 2293 | 22.66% | 9023 | 89.16% |
| 7ª | 0.22 | \|----- | 0.42 | 0.32 | 1097 | 10.84% | 10120 | 100.00% |

Source: Authors (2021).

In this case, a total of seven classes with 0.20 m interval between them were calculated. The most of results are in the class range between 0.02 and 0.22 meters, with a 22.66% relative frequency, followed by the fifth class from -0.18 to 0.02 meters, 20.79% relative frequency, followed by the fourth class with 18.57% relative frequency. Of the 10,120 points analyzed after the refinement, Figure 12 shows that the lowest frequencies are at the edges of the frequency distribution, in classes 1, 2, and 7, with the respective relative frequencies 7.45%, 7.58%, and 10.84%. The position measures were: -0.19 m arithmetic mean, -0.14 m median, and 0.12 meters mode. The dispersion measures for the refined frequency were: 0.26 m mean deviation, 0.34 m standard deviation, 1.02 m maximum error, and 0.12 m variance.

Figure 12 – Frequency Distribution Chart of Refined Discrepancies.

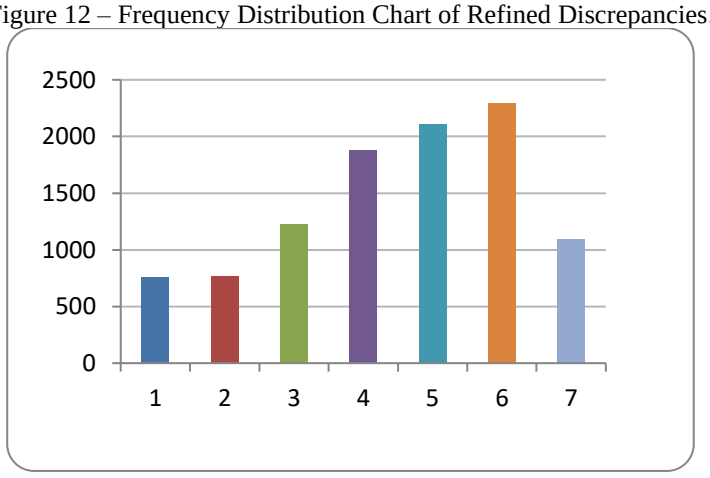


Source: Authors (2021).

### 3.1.6 ALTIMETRIC CORRECTION BY QUADRATIC INTERPOLATION

Following filtering of PPC and PCL clouds in the previous step, Table 11 was generated with the correction of the altimetric difference between the PPC and PCL cloud, as topic 2.2. Table 11 presents 10,121 lines, and to reduce the presentation size, only three lines were placed to exemplify this result (Figure 13). We can see that the blue region of the map is the roof region with the highest altimetric correction in the PPC cloud, and the red region is the soil region with lower altimetric correction in the PPC cloud.

Table 11 – Sample of Altimetric Difference between PPC and PCL Cloud.

| E (m) | N (m) | Correction (m) |
|---|---|---|
| 667,494.62 | 7,177,214.18 | -0.98 |
| 667,941.33 | 7,177,106.76 | -0.05 |
| 667,798.33 | 7,177,438.38 | 0.41 |

Source: Authors (2021).

Figure 13 – PPC to PCL Correction Map.

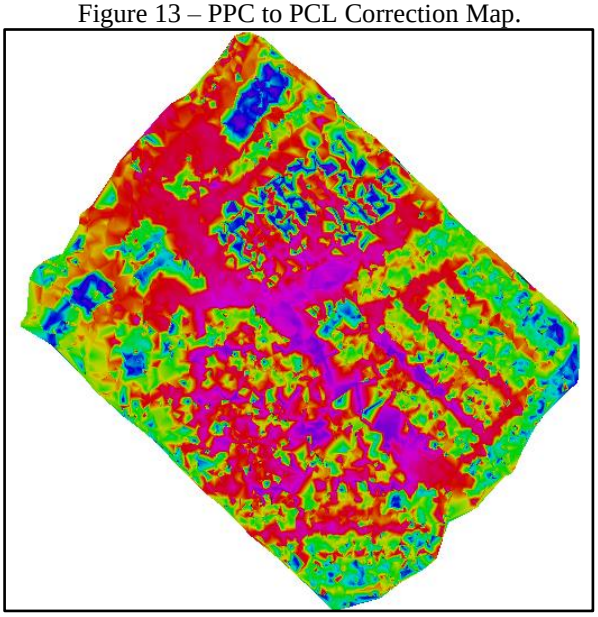

Source: Authors (2021).

### 3.1.7 INTEGRATION OF POINT CLOUDS PPC AND PCL

This step consists of obtaining the integration results of point clouds by applying the correction map generated previously to the point cloud originating from the UAV, adjusting it into the LiDAR point cloud.

Figure 14 - Integrated Clouds after applying the Correction Map.

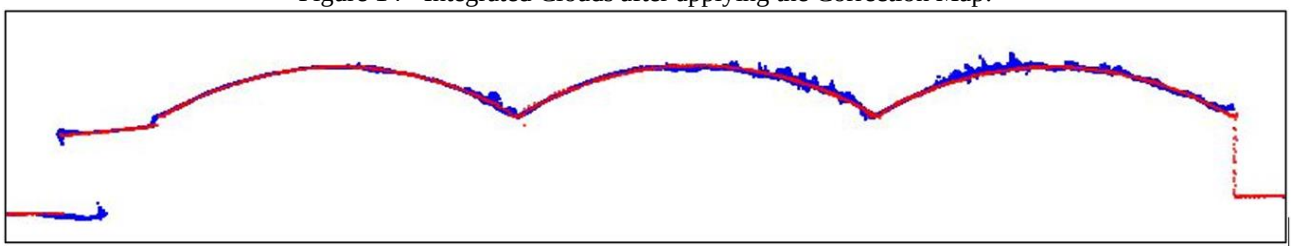

Source: Authors (2021).

Figure 14 illustrates the application of the generated correction map. Concerning the point cloud from the UAV, PPC in blue, the point cloud from the LiDAR was corrected and adjusted, i.e., the PCL in red considered the field truth in this work. As we can see in Figure 15 the integration of clouds (PPC and PCL) significantly improved the definition of building edges for future 3D reconstruction.

Figure 15 – Example of Edge Definition Improvement.

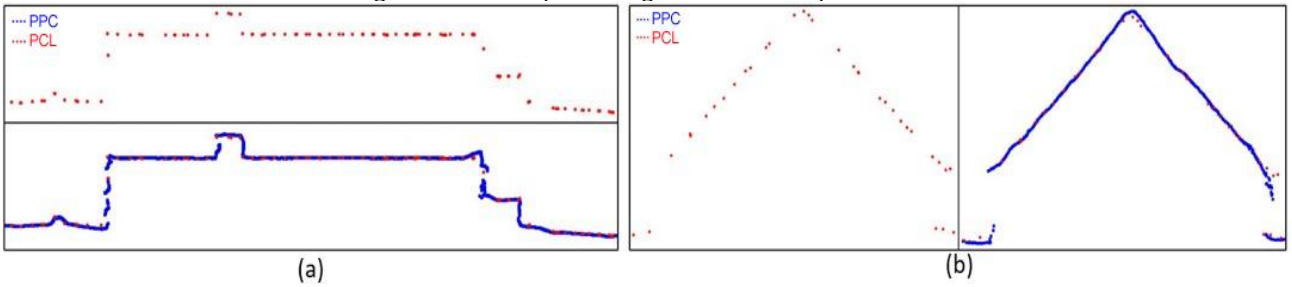


Source: Authors (2021).

Figure 16a shows that integrating clouds (PPC and PCL) significantly minimized occlusion failures for future 3D reconstruction and Figure 16b shows the occurrence of significant densification. Initially the PCL cloud had 2,110,626 points, i.e., 7.7 pts/m², whereas the cloud PPC initially had 33,452,878 points, i.e., 132.7 pts/m².

Figure 16 – (a) Occlusion Failure Minimization and (b) Integration Cloud Densification.

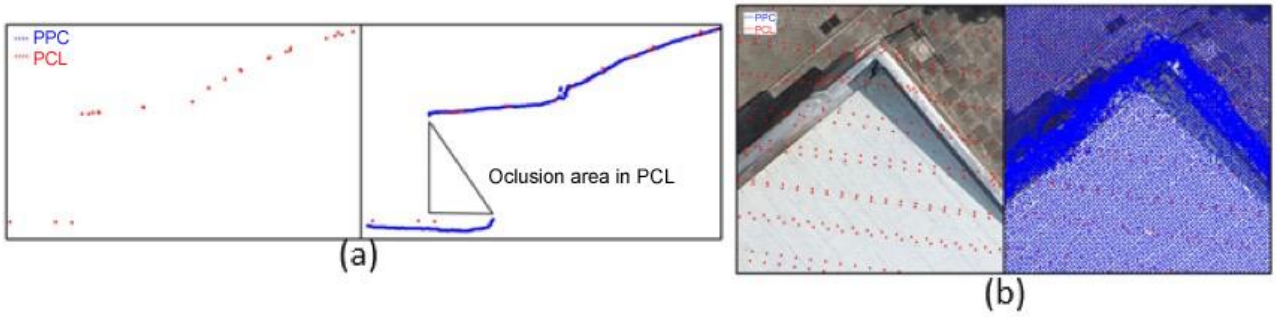


Source: Authors (2021).

The fusion of clouds resulted in a cloud with 35,563,504 points, i.e., 140.4 pts/m². Figure 17a illustrate that the integration of clouds (PPC and PCL) made it possible to locate the spurious points in the PPC cloud more easily, thus significantly improving the classification of point clouds for future 3D reconstruction. Figure 17b shows that the integration of clouds (PPC and PCL) defined the vegetation shape more precisely, thus significantly improving the vegetation classification and consequently improving the three-dimensional modeling of trees in urban areas.

Figure 17 – Example of the (a) Location of Spurious Points and (b) Improved Vegetation Definition.

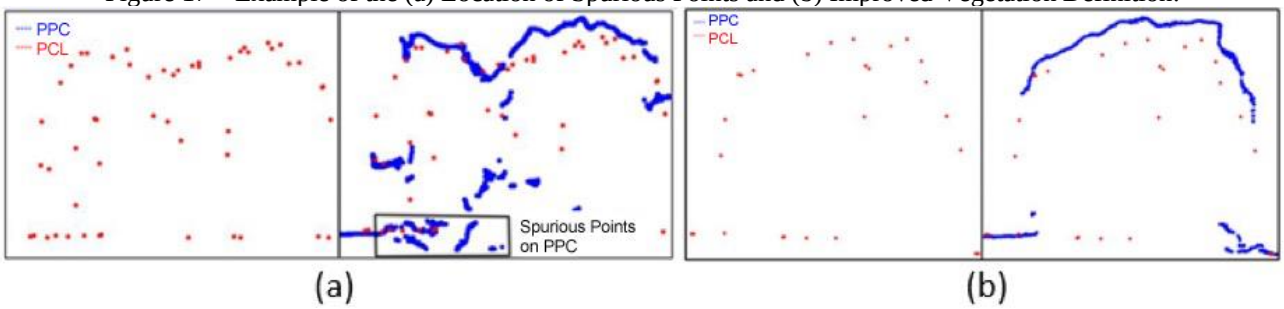


Source: Authors (2021).

## 4 FINAL CONSIDERATIONS

This research presented a methodology for integrating UAV points cloud with LiDAR clouds, obtaining point entities, thus acquiring the control points in photogrammetric processing. Based on the study carried out in this first part, the following conclusions and recommendations are presented:

a) This use of point entities ensured that planimetrically the UAV and LiDAR cloud were compatible, thus carrying out the integration of clouds in planimetry;
b) The general accuracy of the photogrammetric processing showed low residuals for the X, Y, and Z coordinates (centimeter values), demonstrating that the use of point entities met the need for the integration of UAV and LiDAR point clouds;
c) The differences between the UAV and LiDAR point clouds before integration show a pattern, where the UAV cloud, at ground level, has a negative discrepancy on average of twenty centimeters. For roofs, the points reconstructing this feature in the UAV cloud showed a positive discrepancy, on average, one meter. Thus, we can conclude that the photogrammetric processing of the UAV presented a scale factor in the Z component;
d) Integration points were used to correct this scaling factor. These points were located in UAV and LiDAR clouds and required statistical filtering. After the filtering step, we can conclude that the table of the frequency distribution of integration points showed results similar to those observed in the visual comparison of clouds;
e) Filtering UAV and LIDAR clouds enabled us to correct the altimetric difference between the clouds, i.e., the correction map between the clouds. Therefore, we can conclude that using this map with quadratic interpolation allowed us to correct this scale factor presented in Z in the UAV point cloud.

For future works an automatic cloud integration algorithm can be programmed, making it easier for

users to integrate clouds and quickly classify and model. This integration allowed obtaining a denser point cloud than the LiDAR cloud, minimizing occlusion failures, improving the definition of building edges, reducing spurious points, and obtaining a point cloud with better geometric conditions for extraction and modeling cartographic elements. As suggestions for future work: the conduction of other integration tests, such as seven-parameter Isogonal Transformation, the investigation of the altimetric variation in the point cloud generated by UAV aerial survey, application of modeling techniques in the integrated cloud to evaluate the performance of this gain in the density of the LiDAR cloud (PCL) with the UAV cloud (PPC), and performance of point classification tests in the integrated cloud to assess the improvement in densification.

## Author's contribution

Conceptualization, M.A.R.M.; methodology, M.A.R.M. and E.A.M; software, M.A.R.M. and N.D.A; validation, M.A.R.M. and E.A.M; formal analysis, M.A.R.M. and E.A.M; investigation, M.A.R.M.; data curation, M.A.R.M.; writing original draft preparation, M.A.R.M.; visualization, M.A.R.M. and E.A.M; writing review and editing, M.A.R.M. and N.D.A. All authors have read and agreed to the published version of the manuscript.

## Conflict of interest

The authors declare no conflict of interest.

## Referências

BRENNER, C. Building reconstruction from images and laser scanning. **International Journal of Applied Earth Observation and Geoinformation**, v. 6, n. 3–4, p. 187–198, mar. 2005. DOI: 10.1016/j.jag.2004.10.006.

FURUKAWA, Y., HERNÁNDEZ, C.; **Multi-view stereo: A tutorial**. Foundations and Trends in Computer Graphics and Vision, v. 9, n. 1-2, p. 1-148, 2015.

GRUEN, A., BALTSAVIAS, E., HENRICSSON, O. **Automatic Extraction of Man-Made Objects from Aerial and Space Images** (II). 7. ed. [S.l.], Birkhäuser Basel, 1997.

GRUEN, A., KUEBLER, O., AGOURIS, P. **Automatic Extraction of Man-Made Objects from Aerial Space Images**. 5. ed. [S.l.], Birkhäuser Basel, 1995.

HABIB, A. F., ZHAL, R., KIM, C. Generation of complex polyhedral building models by integrating stereo-aerial imagery and lidar data. **Photogrammetric Engineering and Remote Sensing**, v. 76, n. 5, p. 609–623, 2010. DOI: 10.14358/PERS.76.5.609.

IGLHAUT, J.; CABO, C.; PULITI, S.; PIERMATTEI, L.; O'CONNOR, J.; ROSETTE, J.. Structure from Motion Photogrammetry in Forestry: a review. **Current Forestry Reports**, [S.L.], v. 5, n. 3, p. 155-168, 16 jul. 2019. DOI: 1007/s40725-019-00094-3.

KWON, S., PARK, J. W., MOON, D., JUNG, S., Park, H. Smart Merging Method for Hybrid Point Cloud Data using UAV and LiDAR in Earthwork Construction. 196, 1 jan. 2017. **Anais** [...] [S.l.], Elsevier Ltd, 1 jan. 2017. p. 21–28. DOI: 10.1016/j.proeng.2017.07.168.

LESLAR, M. Integrating Terrestrial LiDAR with Point Clouds Created from Unmanned Aerial Vehicle Imagery. **ISPRS - International Archives of the Photogrammetry, Remote Sensing and Spatial Information Sciences**, v. 40, n. 1, p. 97–101. DOI: 10.5194/isprsarchives-XL-1-W4-97-2015.

MARTINS, M. A. R., MITISHITA, E. A. Linear regression and lines intersecting as a method of extracting punctual entities in a lidar point cloud. **Bulletin of Geodetic Sciences**, v. 27, n. 3, 2021. DOI: 10.1590/s1982-21702021000300022.

MOON, D., CHUNG, S., KWON, S., SEO, J., SHIN, J. Comparison and utilization of point cloud generated from photogrammetry and laser scanning: 3D world model for smart heavy equipment planning.

**Automation in Constructio**n, v. 98, p. 322–331, 1 fev. 2018. DOI: 10.1016/j.autcon.2018.07.020.

OLIVEIRA, H. C. **Detecção de áreas de oclusão para geração de ortoimagem verdadeira utilizando dados LASER**. 2013. 95 páginas. Dissertação de Mestrado – Programa de Pós Graduação em Ciências Cartográficas, Universidade Estadual Paulista, Presidente Prudente, 2013.

ŠAŠAK, J., GALLAY, M., KAŇUK, J., HOFIERKA, J., MINÁR, J. Combined Use of Terrestrial Laser Scanning and UAV Photogrammetry in Mapping Alpine Terrain. **Remote Sensing**, v. 11, n. 18, p. 2154, 16 set. 2019. DOI: 10.3390/rs11182154.

SHAN, J., TOTH, C. K. **Topographic Laser Ranging and Scanning**. 2. ed. Boca Raton, CRC Press, 2018.

SMITH, M. J., CHANDLER, J., ROSE, J. High spatial resolution data acquisition for the geosciences: Kite aerial photography. **Earth Surface Processes and Landforms**, v. 34, n. 1, p. 155–161, 2009. DOI: 10.1002/esp.1702.

SNAVELY, N., SEITZ, S. M., SZELISKI, R. Modeling the world from Internet photo collections. **International Journal of Computer Vision**, v. 80, n. 2, p. 189–210, 11 nov. 2008. DOI: 10.1007/s11263-007-0107-3.

SNAVELY, N., SEITZ, S. M., SZELISKI, R. Photo tourism: Exploring photo collections in 3D. **ACM Transactions on Graphics**, v. 25, n. 3, p. 835–846, 1 jul. 2006. DOI: 10.1145/1141911.1141964.

SZABÓ, S., ENYEDI, P., HORVÁTH, M., KOVÁCS, Z., BURAI, P., CSOKNYAI, T., SZABÓ, G. Automated registration of potential locations for solar energy production with Light Detection and Ranging (LiDAR) and small format photogrammetry. **Journal of Cleaner Production**, v. 112, p. 3820–3829, 20 jan. 2016. DOI: 10.1016/j.jclepro.2015.07.117.

ULLMAN, S. The interpretation of structure from motion. **Proceedings of the Royal Society of London. Series B, Containing papers of a Biological character. Royal Society (Great Britain)**, v. 203, n. 1153, p. 405–426, 1979. DOI: 10.1098/rspb.1979.0006.

WESTOBY, M. J., BRASINGTON, J., GLASSER, N. F., HAMBREY, M. J., REYNOLDS, J. M. "Structure-from-Motion" photogrammetry: A low-cost, effective tool for geoscience applications. **Geomorphology**, v. 179, p. 300–314, 2012. DOI: 10.1016/j.geomorph.2012.08.021.

## Biography

Graduated in Cartographic Engineering from Universidade Federal do Paraná (2002), Master's (2010) and Doctorate (2022) in Geodetic Sciences from Universidade Federal do Paraná (UFPR). Is currently a substitute professor at UFPR and has served as a professor of Topography, Geosciences and Statistics at UNICESUMAR and FACEAR. Was operational director at companies Fiducial Engenharia e Aerolevantamentos and Catena Cartografia. Has experience in Geosciences, with emphasis on Photogrammetry and LiDAR, working mainly in following areas: generation of precision cartographic base, digital laser mapping (LiDAR), photogrammetry, "Structure from Motion - SfM", Geodesy and Topography.